MODELING THE INTERACTION OF TERAHERTZ PULSE WITH HEALTHY SKIN AND BASAL CELL CARCINOMA USING THE UNCONDITIONALLY STABLE FUNDAMENTAL ADI-FDTD METHOD

D. Y. Heh[*] and E. L. Tan

School of Electrical and Electronic Engineering, Nanyang Technological University, 50, Nanyang Avenue, Singapore 639798, Singapore

Abstract—This paper presents the application of unconditionally stable fundamental finite-difference time-domain (FADI-FDTD) method in modeling the interaction of terahertz pulse with healthy skin and basal cell carcinoma (BCC). The healthy skin and BCC are modeled as Debye dispersive media and the model is incorporated into the FADI-FDTD method. Numerical experiments on delineating the BCC margin from healthy skin are demonstrated using the FADI-FDTD method based on reflected terahertz pulse. Hence, the FADI-FDTD method provides further insight on the different response shown by healthy skin and BCC under terahertz pulse radiation. Such understanding of the interaction of terahert pulse radiation with biological tissue such as human skin is an important step towards the advancement of future terahertz technology on biomedical applications.

1. INTRODUCTION

Terahertz radiation typically occupies the electromagnetic spectrum between 0.1 THz to 10 THz (1 THz $= 10^{12}$ Hz), and has widespread biomedical application involving the interaction of terahertz pulse with biological media [1–4]. Among them, terahertz radiation has been used successfully as a noninvasive imaging technique for detection of human skin cancer [5–10], in particular, the basal cell carcinoma (BCC). The healthy human skin and BCC have shown different response under the radiation of terahertz pulse and it is possible for terahertz pulse radiation to differentiate between healthy skin and BCC in outlining

the tumour margin prior to surgery, such as the Mohs micrographic surgery (MMS). All these further necessitate a better understanding of the interaction of terahertz pulse with healthy skin and BCC.

The finite-difference time-domain (FDTD) method [11, 12] has been widely used for modeling electromagnetic wave propagation in various media. Since we are mostly interested in the real time information of the terahertz pulse radiation, the time domain based FDTD method appears to be a suitable candidate for modeling the interaction of terahertz pulse with human skin. Unfortunately, the usage of such explicit FDTD method is limited by the fact that its time step is restricted by the Courant-Friedrich-Lewy (CFL) condition, given below as

$$\Delta t \leq \sqrt{\frac{\mu\epsilon}{\frac{1}{\Delta x^2} + \frac{1}{\Delta y^2} + \frac{1}{\Delta z^2}}} \tag{1}$$

where ϵ and μ are the permittivity and permeability of the media, respectively. Δt, Δx, Δy and Δz are the time step and spatial steps in x, y and z-directions, respectively. This restriction results in long simulation time when the spatial steps are small. Nevertheless, some numerical examples involving the interaction of terahertz pulse with human skin in only one dimensional system have been shown in [13] and [14] using this explicit FDTD method.

The modeling in this paper is based on the unconditionally stable fundamental alternating-direction-implicit finite-difference time-domain (FADI-FDTD) method [15], where the time step is no longer restricted by the above CFL condition. It is developed recently not only to remove the stability constraint in (1), but also to address the considerably huge arithmetic operations and memory indexing of the conventional alternating-direction-implicit finite-difference time-domain (ADI-FDTD) method [16, 17]. The FADI-FDTD algorithm is included within a family of fundamental implicit schemes, which feature similar fundamental updating structures that are in simplest forms with most efficient matrix-operator-free right-hand-side. This leads to substantial reduction in arithmetic operations and memory indexing.

In this work, the full three dimensional FADI-FDTD will be employed to model the terahertz pulse interaction with healthy skin and BCC. The healthy skin and BCC are both modeled as Debye dispersive media and the model is then incorporated into our FADI-FDTD method. Numerical experiments on delineating the BCC margin from healthy skin will be demonstrated based on reflected terahertz pulse.

2. HUMAN SKIN AS DEBYE DISPERSIVE MEDIA

It has been shown in [14] that the complex permittivity for both healthy skin and BCC in the terahertz region can be modeled using the Debye dispersive media. The general complex permittivity model of a Debye dispersive medium is described by

$$\epsilon(\omega) = \epsilon_\infty + \sum_p \frac{\Delta\epsilon_p}{1 + j\omega\tau_p} \tag{2}$$

where $j = \sqrt{-1}$, ω is the angular frequency, ϵ_∞ is the relative permittivity at infinite frequency, $\Delta\epsilon_p$ is the change of relative permittivity in p-th Debye pole and τ_p is the p-th pole relaxation time. Note that we have adopted the convention of $e^{j\omega t}$ throughout the paper.

Apart from complex permittivity, the electrical behaviour of a material is frequently described in terms of complex refractive index. The complex refractive index is defined as

$$n(w) = n_r(w) - jn_k(w) \tag{3}$$

where n_r is the real part of the complex refractive index and n_k is known as the extinction coefficient. n_k is related to the absorption coefficient μ_a by

$$n_k = \frac{\mu_a\lambda}{4\pi} \tag{4}$$

where λ is the free space wavelength. The complex refractive index in (3) is simply related to the complex permittivity in (2) by

$$\epsilon(w) = n(w)^2 = n_r(w)^2 - n_k(w)^2 - j2n_r(w)n_k(w). \tag{5}$$

It is found that two Debye poles are sufficient to describe the complex permittivity of healthy skin and BCC in the terahertz region of 0.2 THz to 2 THz [14] and their Debye parameters are tabulated in Table 1. Figure 1 shows the (a) real part of complex refractive index, n_r and (b) absorption coefficient, μ_a versus frequency for healthy skin and BCC. We can see that BCC generally has higher n_r and μ_a than healthy skin throughout the terahertz region. It is anticipated that

Table 1. Debye parameters for healthy skin and BCC in terahertz region.

	ϵ_∞	$\Delta\epsilon_1$	$\Delta\epsilon_2$	τ_1/ps	τ_2/ps
healthy skin	2.58	10.54	1.58	1.45	0.0611
BCC	2.65	13.37	1.58	1.55	0.0614
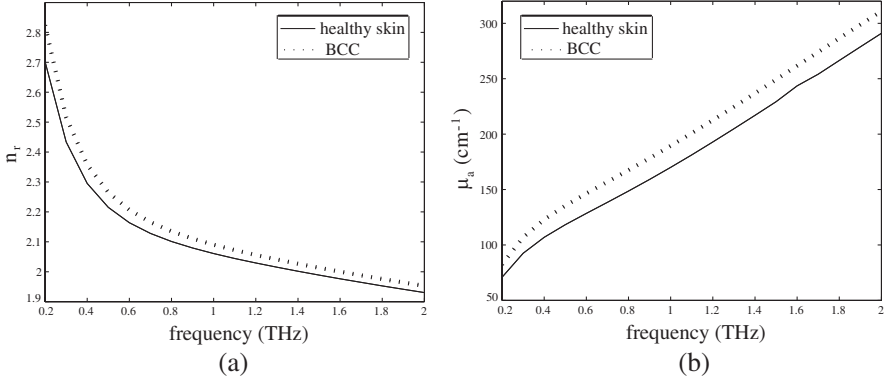
Figure 1. (a) Real part of complex refractive index, n_r. (b) Absorption coefficient, μ_a versus frequency for healthy skin and BCC. BCC generally has higher n_r and μ_a than healthy skin throughout the terahertz region.

with a difference in both n_r and μ_a between healthy skin and BCC, they will exhibit different response under terahertz pulse radiation. The different terahertz pulse radiation response shall be demonstrated in the subsequent sections.

3. INCORPORATION INTO THE FUNDAMENTAL ADI-FDTD (FADI-FDTD) METHOD

In this section, the Debye dispersive model is incorporated into the FADI-FDTD. For completeness, we include the implementation of magnetic Debye dispersive model with permeability at infinite frequency μ_∞, change in relative permeability $\Delta\mu$ and magnetic relaxation time τ'. To that end, the Maxwell's curl equations with both electric and magnetic Debye dispersive models are given by

$$\nabla \times \mathbf{H}(t) = \epsilon_0\epsilon_\infty\frac{\partial}{\partial t}\mathbf{E}(t)+\sigma\mathbf{E}(t)+\epsilon_0\sum_p \mathcal{F}^{-1}\left\{j\omega\frac{\Delta\epsilon_p}{1+j\omega\tau_p}\mathbf{E}(\omega)\right\}$$

$$= \epsilon_0\epsilon_\infty\frac{\partial}{\partial t}\mathbf{E}(t)+\sigma\mathbf{E}(t)+\sum_p \mathbf{J}_p(t) \tag{6a}$$

$$-\nabla \times \mathbf{E}(t) = \mu_0\mu_\infty\frac{\partial}{\partial t}\mathbf{H}(t)+\sigma^*\mathbf{H}(t)+\mu_0\sum_p \mathcal{F}^{-1}\left\{j\omega\frac{\Delta\mu_p}{1+j\omega\tau'_p}\mathbf{H}(\omega)\right\}$$

$$= \mu_0\mu_\infty\frac{\partial}{\partial t}\mathbf{H}(t)+\sigma^*\mathbf{H}(t)+\sum_p \mathbf{M}_p(t) \tag{6b}$$

where ϵ_0 and μ_0 are the permittivity and permeability in free space, σ and σ^* are the electric and magnetic conductivities, respectively. The symbol $\mathcal{F}^{-1}$ denotes inverse Fourier transform operation and two auxiliary variables $\mathbf{J}_p$ and $\mathbf{M}_p$ are introduced. These auxiliary variables are related to electric and magnetic fields in time domain by the following relations:

$$\tau_p \frac{\partial}{\partial t}\mathbf{J}_p(t) + \mathbf{J}_p(t) \,=\, \epsilon_0 \Delta \epsilon_p \frac{\partial}{\partial t}\mathbf{E}(t) \tag{7a}$$

$$\tau_p' \frac{\partial}{\partial t}\mathbf{M}_p(t) + \, \mathbf{M}_p(t) \,=\, \mu_0 \Delta \mu_p \frac{\partial}{\partial t}\mathbf{H}(t). \tag{7b}$$

Discretizing (7) using central difference approximation around time index $n + \frac{1}{4}$, we obtain the following difference equations:

$$\mathbf{J}_p^{n+\frac{1}{2}} \,=\, k_{1p}\mathbf{J}_p^n + k_{2p}\left(\mathbf{E}^{n+\frac{1}{2}} - \mathbf{E}^n\right), \tag{8a}$$

$$\mathbf{M}_p^{n+\frac{1}{2}} \,=\, l_{1p}\mathbf{M}_p^n + l_{2p}\left(\mathbf{H}^{n+\frac{1}{2}} - \mathbf{H}^n\right). \tag{8b}$$

where

$$k_{1p} \,=\, \frac{1 - \frac{\Delta t}{4\tau_p}}{1 + \frac{\Delta t}{4\tau_p}}, \qquad k_{2p} \,=\, \frac{\epsilon_0 \Delta \epsilon_p / \tau_p}{1 + \frac{\Delta t}{4\tau_p}}, \tag{9a}$$

$$l_{1p} \,=\, \frac{1 - \frac{\Delta t}{4\tau_p'}}{1 + \frac{\Delta t}{4\tau_p'}}, \qquad l_{2p} \,=\, \frac{\mu_0 \Delta \mu_p / \tau_p'}{1 + \frac{\Delta t}{4\tau_p'}}. \tag{9b}$$

Note that the time step used in the central difference approximation is only $\Delta t/2$ to accomodate the two-substeps nature of the FADI-FDTD with each substep having the time step of $\Delta t/2$.

Prior to formulating the FADI-FDTD, we first write down the update procedures of the conventional ADI-FDTD in compact matrix form as

$$(\mathbf{I}_{12} - \mathbf{D}_2\mathbf{A} + \mathbf{F}_l)\mathbf{u}^{n+\frac{1}{2}} \,=\, (\mathbf{D}_1 + \mathbf{D}_2\mathbf{B} + \mathbf{F}_r)\mathbf{u}^n + \mathbf{D}_2\mathbf{s}^{n+\frac{1}{2}} \tag{10a}$$

$$(\mathbf{I}_{12} - \mathbf{D}_2\mathbf{B} + \mathbf{F}_l)\mathbf{u}^{n+1} \,=\, (\mathbf{D}_1 + \mathbf{D}_2\mathbf{A} + \mathbf{F}_r)\mathbf{u}^{n+\frac{1}{2}} + \mathbf{D}_2\mathbf{s}^{n+\frac{1}{2}} \tag{10b}$$

where

$$\mathbf{u} \,=\, [E_x, E_y, E_z, H_x, H_y, H_z, J_x, J_y, J_z, M_x, M_y, M_z,]^T \tag{11}$$

$$\mathbf{s} \,=\, [-s_{ex}, \, -s_{ey}, \, -s_{ez}, 0, \, 0, \, 0, \, 0, \, 0, \, 0, \, 0, \, 0, \, 0]^T \tag{12}$$

$$
\mathbf{A} = \begin{bmatrix} \mathbf{O}_3 & \mathbf{K}1 & \mathbf{O}_3 & \mathbf{O}_3 \\ \mathbf{K}_2 & \mathbf{O}_3 & \mathbf{O}_3 & \mathbf{O}_3 \\ \mathbf{O}_3 & \mathbf{O}_3 & \mathbf{O}_3 & \mathbf{O}_3 \\ \mathbf{O}_3 & \mathbf{O}_3 & \mathbf{O}_3 & \mathbf{O}_3 \end{bmatrix}, \qquad \mathbf{B} = \begin{bmatrix} \mathbf{O}_3 & -\mathbf{K}_2 & \mathbf{O}_3 & \mathbf{O}_3 \\ -\mathbf{K}_1 & \mathbf{O}_3 & \mathbf{O}_3 & \mathbf{O}_3 \\ \mathbf{O}_3 & \mathbf{O}_3 & \mathbf{O}_3 & \mathbf{O}_3 \\ \mathbf{O}_3 & \mathbf{O}_3 & \mathbf{O}_3 & \mathbf{O}_3 \end{bmatrix} \quad (13)
$$

$$
\mathbf{K}_1 = \begin{bmatrix} 0 & 0 & \frac{\partial}{\partial y} \\ \frac{\partial}{\partial z} & 0 & 0 \\ 0 & \frac{\partial}{\partial x} & 0 \end{bmatrix}, \qquad \mathbf{K}_2 = \begin{bmatrix} 0 & \frac{\partial}{\partial z} & 0 \\ 0 & 0 & \frac{\partial}{\partial x} \\ \frac{\partial}{\partial y} & 0 & 0 \end{bmatrix} \qquad (14)
$$

$$
\mathbf{D}_1 = \mathrm{diag}(c_1, c_1, c_1, d_1, d_1, d_1, k_1, k_1, k_1, l_1, l_1, l_1,) \qquad (15)
$$

$$
\mathbf{D}_2 = \mathrm{diag}(c_2, c_2, c_2, d_2, d_2, d_2, 0, 0, 0, 0, 0, 0) \qquad (16)
$$

$$
\mathbf{F}_l = \begin{bmatrix} \mathbf{O}_3 & \mathbf{O}_3 & \mathbf{O}_3 & \mathbf{O}_3 \\ \mathbf{O}_3 & \mathbf{O}_3 & \mathbf{O}_3 & \mathbf{O}_3 \\ -k_2\mathbf{I}_3 & \mathbf{O}_3 & \mathbf{O}_3 & \mathbf{O}_3 \\ \mathbf{O}_3 & -l_2\mathbf{I}_3 & \mathbf{O}_3 & \mathbf{O}_3 \end{bmatrix} \qquad (17)
$$

$$
\mathbf{F}_r = \begin{bmatrix} \mathbf{O}_3 & \mathbf{O}_3 & -c_2\frac{1}{2}(1+k_1)\mathbf{I}_3 & \mathbf{O}_3 \\ \mathbf{O}_3 & \mathbf{O}_3 & \mathbf{O}_3 & -d_2\frac{1}{2}(1+l_1)\mathbf{I}_3 \\ k_2\mathbf{I}_3 & \mathbf{O}_3 & \mathbf{O}_3 & \mathbf{O}_3 \\ \mathbf{O}_3 & l_2\mathbf{I}_3 & \mathbf{O}_3 & \mathbf{O}_3 \end{bmatrix} \qquad (18)
$$

$\mathbf{I}_r$ and $\mathbf{O}_r$ represent identity and null matrices with dimension $r \times r$. Coefficients c_1, c_2, d_1, and d_2 are defined as

$$
c_1 = \frac{1 - \frac{\sigma \Delta t}{4\epsilon_0 \epsilon_\infty} + \frac{\Delta t}{4\epsilon_0 \epsilon_\infty} \sum_p k_{2p}}{1 + \frac{\sigma \Delta t}{4\epsilon_0 \epsilon_\infty} + \frac{\Delta t}{4\epsilon_0 \epsilon_\infty} \sum_p k_{2p}}, \quad c_2 = \frac{\frac{\Delta t}{2\epsilon_0 \epsilon_\infty}}{1 + \frac{\sigma \Delta t}{4\epsilon_0 \epsilon_\infty} + \frac{\Delta t}{4\epsilon_0 \epsilon_\infty} \sum_p k_{2p}}, \quad (19\mathrm{a})
$$

$$
d_1 = \frac{1 - \frac{\sigma^* \Delta t}{4\mu_0 \mu_\infty} + \frac{\Delta t}{4\mu_0 \mu_\infty} \sum_p l_{2p}}{1 + \frac{\sigma^* \Delta t}{4\mu_0 \mu_\infty} + \frac{\Delta t}{4\mu_0 \mu_\infty} \sum_p l_{2p}}, \quad d_2 = \frac{\frac{\Delta t}{2\mu_0 \mu_\infty}}{1 + \frac{\sigma^* \Delta t}{4\mu_0 \mu_\infty} + \frac{\Delta t}{4\mu_0 \mu_\infty} \sum_p l_{2p}}, \quad (19\mathrm{b})
$$

Electric current sources s_{ex}, s_{ey} and s_{ez} are also included in the formulation. Note that in the compact matrix form, we assume only single pole Debye model, but they can be systematically expanded for multiple Debye poles in the update equations.

Now, to formulate FADI-FDTD, introducing an auxiliary variable $\tilde{\mathbf{v}}$, (10) is rewritten as

$$
\tilde{\mathbf{v}}^n = (\mathbf{D}_1 + \mathbf{D}_2\mathbf{B} + \mathbf{F}_r)\,\mathbf{u}^n \qquad (20\mathrm{a})
$$

$$
(\mathbf{I}_{12} - \mathbf{D}_2\mathbf{A} + \mathbf{F}_l)\mathbf{u}^{n+\frac{1}{2}} = \tilde{\mathbf{v}}^n + \mathbf{D}_2 s^{n+\frac{1}{2}} \qquad (20\mathrm{b})
$$

$$
\tilde{\mathbf{v}}^{n+\frac{1}{2}} = (\mathbf{D}_1 + \mathbf{D}_2\mathbf{A} + \mathbf{F}_r)\mathbf{u}^{n+\frac{1}{2}} + \mathbf{D}_2 s^{n+\frac{1}{2}} \qquad (20\mathrm{c})
$$

$$
(\mathbf{I}_{12} - \mathbf{D}_2\mathbf{B} + \mathbf{F}_l)\mathbf{u}^{n+1} = \tilde{\mathbf{v}}^{n+\frac{1}{2}} \qquad (20\mathrm{d})
$$

Next, (20d) is expressed at one time step backward as

$$\tilde{\mathbf{v}}^{n-\frac{1}{2}} = (\mathbf{I}_{12} - \mathbf{D}_2\mathbf{B} + \mathbf{F}_l)\mathbf{u}^n \tag{21}$$

and (20a) can be subsequently reduced into

$$
\begin{aligned}
\tilde{\mathbf{v}}^n &= (\mathbf{D}_1 + \mathbf{D}_2\mathbf{B} + \mathbf{F}_r)\mathbf{u}^n \\
&= [(\mathbf{I}_{12} + \mathbf{D}_1) + \mathbf{F}_l + \mathbf{F}_r]\mathbf{u}^n - (\mathbf{I}_{12} - \mathbf{D}_2\mathbf{B} + \mathbf{F}_l)\mathbf{u}^n \\
&= [(\mathbf{I}_{12} + \mathbf{D}_1) + \mathbf{F}_l + \mathbf{F}_r]\mathbf{u}^n - \tilde{\mathbf{v}}^{n-\frac{1}{2}}
\end{aligned}
\tag{22}
$$

Similarly, by rewriting (20b) as

$$\tilde{\mathbf{v}}^n = (\mathbf{I}_{12} - \mathbf{D}_2\mathbf{A} + \mathbf{F}_l)\mathbf{u}^{n+\frac{1}{2}} - \mathbf{D}_2\mathbf{s}^{n+\frac{1}{2}}, \tag{23}$$

(20c) is reducible to

$$
\begin{aligned}
\tilde{\mathbf{v}}^{n+\frac{1}{2}} &= (\mathbf{D}_1 + \mathbf{D}_2\mathbf{A} + \mathbf{F}_r)\mathbf{u}^{n+\frac{1}{2}} + \mathbf{D}_2\mathbf{s}^{n+\frac{1}{2}} \\
&= [(\mathbf{I}_{12}+\mathbf{D}_1) + \mathbf{F}_l + \mathbf{F}_r]\mathbf{u}^{n+\frac{1}{2}} \\
&\quad - \left[(\mathbf{I}_{12} - \mathbf{D}_2\mathbf{A} + \mathbf{F}_l)\,\mathbf{u}^{n+\frac{1}{2}} - \mathbf{D}_2\mathbf{s}^{n+\frac{1}{2}}\right] \\
&= [(\mathbf{I}_{12} + \mathbf{D}_1) + \mathbf{F}_l + \mathbf{F}_r]\,\mathbf{u}^{n+\frac{1}{2}} - \tilde{\mathbf{v}}^n
\end{aligned}
\tag{24}
$$

Finally, the fundamental ADI-FDTD update procedures read:

$$\tilde{\mathbf{v}}^n = [(\mathbf{I}_{12} + \mathbf{D}_1) + \mathbf{F}_l + \mathbf{F}_r]\mathbf{u}^n - \tilde{\mathbf{v}}^{n-\frac{1}{2}} \tag{25a}$$

$$(\mathbf{I}_{12} - \mathbf{D}_2\mathbf{A} + \mathbf{F}_l)\mathbf{u}^{n+\frac{1}{2}} = \tilde{\mathbf{v}}^n + \mathbf{D}_2\mathbf{s}^{n+\frac{1}{2}} \tag{25b}$$

$$\tilde{\mathbf{v}}^{n+\frac{1}{2}} = [(\mathbf{I}_{12} + \mathbf{D}_1) + \mathbf{F}_l + \mathbf{F}_r]\mathbf{u}^{n+\frac{1}{2}} - \tilde{\mathbf{v}}^n \tag{25c}$$

$$(\mathbf{I}_{12} - \mathbf{D}_2\mathbf{B} + \mathbf{F}_l)\mathbf{u}^{n+1} = \tilde{\mathbf{v}}^{n+\frac{1}{2}} \tag{25d}$$

(25a) and (25b) form the first substep while (25c) and (25d) form the second. It is worth noting that the fundamental ADI-FDTD has matrix-operator-free RHS, i.e., there is no matrix operator $\mathbf{A}$ and $\mathbf{B}$ on the RHS of (25). The source excitation is also only needed at the first substep [18] which further simplifies the implementation compared to the conventional ADI-FDTD method.

Letting

$$\tilde{v} = [\tilde{e}_x, \tilde{e}_y, \tilde{e}_z, \tilde{h}_x, \tilde{h}_y, \tilde{h}_z, \tilde{j}_x, \tilde{j}_y, \tilde{j}_z, \tilde{m}_x, \tilde{m}_y, \tilde{m}_z]^T, \tag{26}$$

the update equations of FADI-FDTD for the first substep now read:

$$\tilde{e}_\xi^n = (1 + c_1)E_\xi^n - \tilde{e}_x^{n-\frac{1}{2}} - c_2 \sum_p \frac{1}{2}(1 + k_{1p})J_{\xi p}^n, \quad \xi = x, y, z \quad (27a)$$

$$\tilde{h}_\xi^n = (1 + d_1)H_\xi^n - \tilde{h}_x^{n-\frac{1}{2}} - d_2 \sum_p \frac{1}{2}(1 + l_{1p})M_{\xi p}^n, \quad \xi = x, y, z \quad (27b)$$

$$\tilde{j}_{\xi p}^n = (1 + k_{1p})J_{\xi p}^n - \tilde{j}_{\xi p}^{n-\frac{1}{2}} - 2k_{2p}E_\xi^n, \quad \forall p, \quad \xi = x, y, z \quad (27c)$$

$$\tilde{m}_{\xi p}^n = (1 + l_{1p})M_{\xi p}^n - \tilde{m}_{\xi p}^{n-\frac{1}{2}} - 2l_{2p}H_\xi^n, \quad \forall p, \quad \xi = x, y, z \quad (27d)$$

$$E_x^{n+\frac{1}{2}} - c_2\frac{\partial}{\partial y}H_z^{n+\frac{1}{2}} = \tilde{e}_x^n - c_2 s_{ex}^{n+\frac{1}{2}} \quad (27e)$$

$$E_y^{n+\frac{1}{2}} - c_2\frac{\partial}{\partial z}H_x^{n+\frac{1}{2}} = \tilde{e}_y^n - c_2 s_{ey}^{n+\frac{1}{2}} \quad (27f)$$

$$E_z^{n+\frac{1}{2}} - c_2\frac{\partial}{\partial x}H_y^{n+\frac{1}{2}} = \tilde{e}_z^n - c_2 s_{ez}^{n+\frac{1}{2}} \quad (27g)$$

$$H_x^{n+\frac{1}{2}} - d_2\frac{\partial}{\partial z}E_y^{n+\frac{1}{2}} = \tilde{h}_x^n \quad (27h)$$

$$H_y^{n+\frac{1}{2}} - d_2\frac{\partial}{\partial x}E_z^{n+\frac{1}{2}} = \tilde{h}_y^n \quad (27i)$$

$$H_z^{n+\frac{1}{2}} - d_2\frac{\partial}{\partial y}E_x^{n+\frac{1}{2}} = \tilde{h}_z^n \quad (27j)$$

$$J_{\xi p}^{n+\frac{1}{2}} = k_{2p}E_\xi^{n+\frac{1}{2}} + \tilde{j}_{\xi p}^n, \quad \forall p, \quad \xi = x, y, z \quad (27k)$$

$$M_{\xi p}^{n+\frac{1}{2}} = l_{2p}H_\xi^{n+\frac{1}{2}} + \tilde{m}_{\xi p}^n, \quad \forall p, \quad \xi = x, y, z \quad (27l)$$

The update equations for the second substep can be systematically written down by cyclically switching the subscript of the main field components and space derivatives in (27e)–(27j). Note that the electrical sources, s_{ex}, s_{ey} and s_{ez} will only be needed in the first substep above and shall not be included in the second substep [18]. Since J and M fields are not required in output, (27k) and (27l) can be further substituted into (27a), (27b), (27c) and (27d) in the second substep for more efficiency and simplicity to yield

$$\tilde{e}_\xi^{n+\frac{1}{2}} = \left[1 + c_1 - c_2 \sum_p \frac{1}{2}(1 + k_{1p})k_{2p}\right]E_\xi^{n+\frac{1}{2}} - \tilde{e}_\xi^n$$

$$-c_2 \sum_p \frac{1}{2}(1 + k_{1p})\tilde{j}_{\xi p}^n \quad (28)$$

$$\tilde{h}_\xi^{n+\frac{1}{2}} = \left[1 + d_1 - d_2 \sum_p \frac{1}{2}(1 + l_{1p})l_{2p}\right]H_\xi^{n+\frac{1}{2}} - \tilde{h}_\xi^n$$
$$-c_2 \sum_p \frac{1}{2}(1 + l_{1p})\tilde{m}_{\xi p}^n \tag{29}$$

$$\tilde{j}_{\xi p}^{n+\frac{1}{2}} = k_{2p}(k_{1p} - 1)E_\xi^{n+\frac{1}{2}} + k_{1p}\tilde{j}_{\xi p}^n, \quad \forall p, \quad \xi = x, y, z \tag{30}$$

$$\tilde{m}_{\xi p}^{n+\frac{1}{2}} = l_{2p}(l_{1p} - 1)H_\xi^{n+\frac{1}{2}} + l_{1p}\tilde{m}_{\xi p}^n, \quad \forall p, \quad \xi = x, y, z \tag{31}$$

4. INTERACTION OF TERAHERTZ PULSE WITH HEALTHY SKIN AND BCC EX VIVO

4.1. Reflected Terahertz Pulse

We now demonstrate the use of FADI-FDTD in the simulation of human skin *ex vivo*. Half-spaced healthy skin and BCC are considered separately and they are subjected to illumination by Gaussian pulse with frequency content of up to 2 THz. Cell size is set at 1.8 μm which resolves around 1/40 times the wavelength in the human skin at 2 THz. The time step Δt is specified as Courant-Friedrich-Lewy number (CFLN), which is relative to the Courant-Friedrich-Lewy time step limit in the explicit Yee's FDTD method, i.e., $CFLN = \Delta t/\Delta t_{\mathrm{CFL}}$ where Δt_{CFL} is the maximum allowed time step of explicit FDTD method in (1). In this case, we choose CFLN = 10. The healthy skin and BCC both have Debye parameters adopted from Table 1. The terahertz pulse is incident upon the human skin from a quartz medium having a constant relative permittivity of 4.5 [14]. The quartz-skin interface is considered because the skin samples are placed between sample holders made of quartz during imaging [6]. The terahertz pulse, upon incident at the surface of the human skin, undergoes reflection. The reflected terahertz pulse from healthy skin and BCC is observed and recorded.

After the reflected terahertz pulse is recorded, signal post-processing procedure similar to that in [6] is applied. The reflected terahertz pulse is Fourier transformed into frequency domain $\tilde{E}^r(f)$, and divided by $\tilde{E}^{\mathrm{air}}(f)$, obtained from the reflected terahertz pulse off a quartz-air interface. Subsequently, windowing transfer function or filter is multiplied to it. The post-processed electric field in frequency domain $\tilde{E}(f)$ is given by

$$\tilde{E}(f) = \frac{\tilde{E}^r(f)}{\tilde{E}^{\mathrm{air}}(f)} \times \tilde{W}(f). \tag{32}$$

Finally inverse Fourier transform is applied to $\tilde{E}(f)$ to obtain the final post-processed electric field in time domain as

$$E(t) = \mathcal{F}^{-1}\left\{\tilde{E}(f)\right\}. \tag{33}$$

Note that the post-processing procedure is applied so that the impulse response of the human skin can be obtained.

Figure 2 shows the post-processed terahertz pulse (electric field) from healthy skin and BCC. In this figure, the filter chosen is a Gaussian function with frequency content of up to 2 THz. We first observe that the post-processed electric field is negative. In the quartz-skin interface, the terahertz pulse is reflected off human skin which has generally higher refractive index compared to the incident medium quartz. On the other hand, in the quartz-air interface, the terahertz pulse is reflected off air which has lower refractive index compared to the incident medium quartz. This results in opposite phase between these two reflected terahertz pulse, and hence negative post-processed electric field. It can be seen that the reflected terahertz pulse from BCC has a larger amplitude (more negative) than the reflected terahertz pulse from healthy skin. Since the difference in the refractive index between BCC and quartz is higher than that of healthy skin and quartz (c.f. Figure 1), the terahertz pulse is reflected more from BCC compared to that of healthy skin. The simulation obtained using the Yee's explicit FDTD method is also provided for comparison. It is
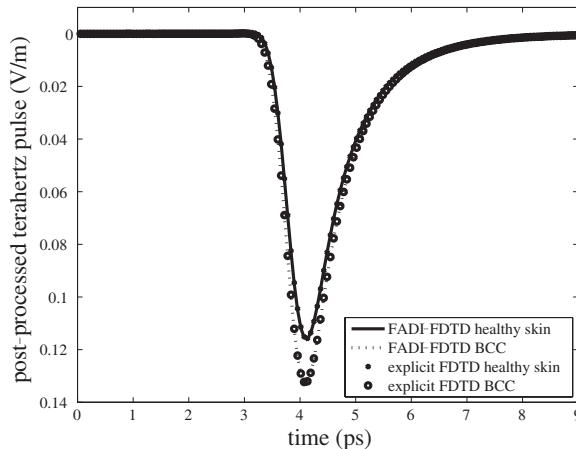
Figure 2. Post-processed terahertz pulse from healthy skin and BCC computed using FADI-FDTD and explicit FDTD. The reflected terahertz pulse from BCC has a larger amplitude than the reflected terahertz pulse from healthy skin.
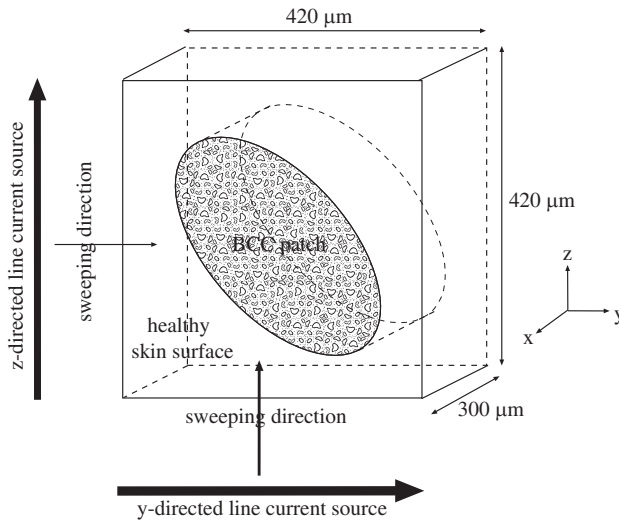
Figure 3. Illustration of the numerical scanning process and geometrical setup of human skin model.

observed that at CFLN = 10 (time step 10 times larger), the FADI-FDTD and Yee's excplicit FDTD methods are in excellent agreement with each other. Furthermore, it is also in agreement with the result shown in past literature, c.f. Figure 3 in [14]. Hence, it can be found that the reflected terahertz pulse can be used to distinguish between a healthy skin and BCC.

4.2. BCC Detection Based on Reflected Terahertz Pulse

With such a difference in reflected terahertz pulse between healthy skin and BCC, we next demonstrate numerical examples of BCC detection based on terahertz pulse illumination using the FADI-FDTD method. The numerical scanning process using the terahertz pulse illumination and geometrical setup of the human skin model are shown in Figure 3. Let the depth of the skin oriented along the x-direction. A z-directed line current source, s_{ez} is oriented parallel to the skin surface and it is scanned along the skin surface in the y-direction. The scanning area is chosen to be $420\,\mu m \times 420\,\mu m$. While the line current source is scanned along the skin surface, the reflected terahertz pulse from each and every point of the skin surface is also collected at the same time. The scanning proceeds until the entire skin surface area is completed. After that, the post-processing procedure as detailed before is applied. The filter is now chosen to be modulated Gaussian function with

frequency content of 0.2 to 2 THz. It is more appropriate compared to the Gaussian function in previous subsection as the two-pole Debye media used to describe the human skin is within terahertz range of 0.2 to 2 THz. Based on the post-processed reflected terahertz pulse of each point, the post-processed peak-to-peak of z-directed electric field, E_{zpp} is extracted.

The procedure is repeated with the z-directed line current source replaced by a y-directed line current source, s_{ey} and it is now scanned along the skin surface in the z-direction. Now, the post-processed peak-to-peak of y-directed electric field, E_{ypp} is extracted. Using the results of the reflected terahertz pulse from two line current sources (z-directed and y-directed), we obtain the overall post-processed peak-to-peak electric field, E_{pp} by

$$E_{pp} = \frac{1}{2}(E_{zpp} + E_{ypp}). \tag{34}$$

Note that we take the average value of the post-processed peak-to-peak terahertz pulse obtained by these two line current sources. By doing so, the characteristics of the reflected pulse from two orthogonal line current sources can be taken into consideration. Furthermore, by using two orthogonal line current sources, only two "sweeps" are needed in two orthogonal directions to complete the scanning process for the entire surface area of the skin. This is far more efficient than the conventional way of point by point scanning. The use of lenses for focusing the terahertz laser beam in the point by point scanning procedure is also redundant. This further simplifies the whole scanning process.

BCC originates from the basal layer of the epidermis, the top most layer of the human skin. Typically, the human epidermis has an average thickness of around 100 μm [19, 20]. In our numerical scanning example, the human skin consists of a 300 μm thick healthy skin and a patch of BCC, also with thickness 300 μm encapsulated within the healthy skin. With a patch thickness of 300 μm, the BCC is assumed to infect the entire layer of epidermis, and extending into the dermis layer, which is the second layer of human skin after epidermis. The patch of BCC has a circular cross sectional area with a radius of 150 μm. Looking from the top, the circular patch of BCC is surrounded by healthy skin tissue. Uniform cell size ($\Delta x = \Delta y = \Delta z$) is now set at 6 μm which resolves around 1/15 times the wavelength in the human skin at 2 THz. The time step, on the other hand is chosen at CFLN = 4. The perfectly matched layer [21] is used to terminate the computational boundaries.

Figure 4(a) plots the numerically scanned image of the overall post-processed peak-to-peak terahertz pulse, E_{pp}, normalized to the
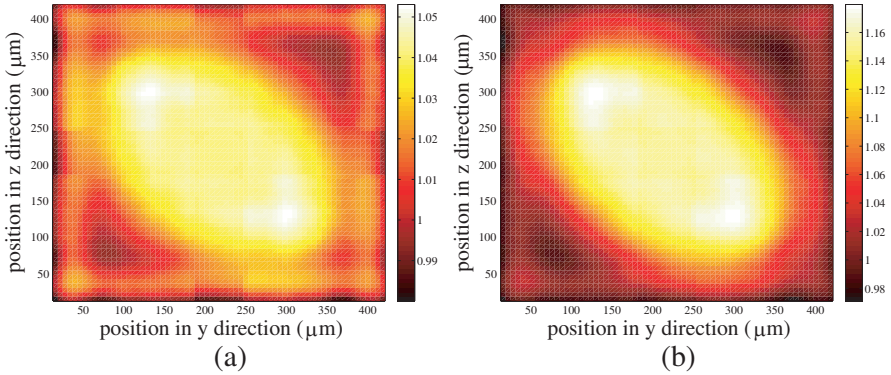
reference post-processed peak-to-peak terahertz pulse, $E_{pp(ref)}$ for the circular BCC patch. Note that this reference is obtained from a confirmed healthy skin. As such, region with value of one indicates that of a healthy skin tissue. From Figure 4(a), the BCC patch with circular cross sectional area of radius $150\,\mu m$ can be clearly seen and E_{pp} exhibited by the BCC is around 10 percent more than that of the surrounding healthy skin tissue. To consider different shape pattern of the BCC cross sectional area, the BCC patch of circular cross sectional area is replaced with BCC patch of elliptic cross sectional
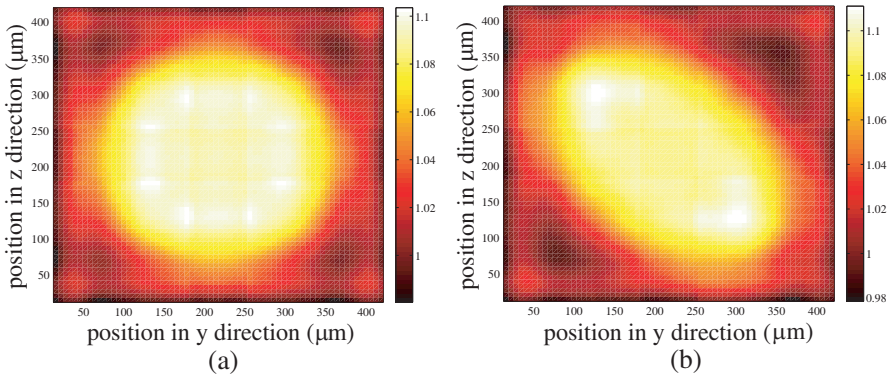
Figure 4. Numerically scanned images of the normalized overall post-processed peak-to-peak terahertz pulse, E_{pp} for (a) BCC patch with circular cross sectional area and (b) BCC patch with 45 degree counter-clockwise rotated elliptic cross sectional area. Region with value of one indicates that of a healthy skin tissue.
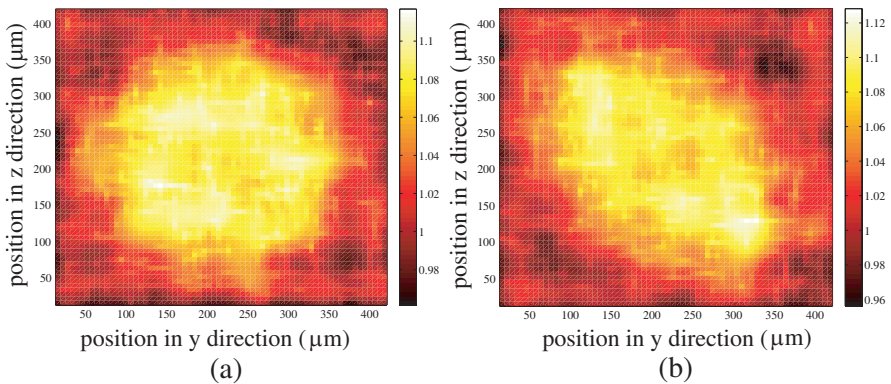
Figure 5. Same as Figure 4, but with roughness and irregularities on the surface of the human skin and edges of BCC patch.

Figure 6. Numerically scanned images of the normalized overall post-processed peak-to-peak terahertz pulse of elliptical BCC patch embedded within healthy skin with Debye parameters fitted to (a) maximum and (b) minimum experimental data.

area. The major and minor semi-axes of the ellipse are oriented along z and y axes respectively, and their respective lengths are $180\,\mu$m and $120\,\mu$m. On top of that, the BCC patch of elliptic cross sectional area is also rotated 45 degree counter-clockwise. Figure 4(b) shows the numerically scanned image of the normalized overall reflected peak-to-peak terahertz pulse for the aforementioned BCC patch. A 45 degree counter-clockwise rotated elliptic cross sectional area with major and minor semi-axes of $180\,\mu$m and $120\,\mu$m can be clearly identified. E_{pp} of the BCC is also 10 percent more than that of the surrounding healthy skin tissue. We further consider surface roughness and structure irregularities in the human skin. Figure 5 shows the numerical scanned images of the same BCC patches in Figure 4, but with some roughness and irregularities randomly introduced on the surface of the human skin and edges of BCC patch. It is observed that the BCC patches are still visible, albeit some irregularities in the margin and contrast. The contrast between BCC and its surrounding healthy tissue is also approximately 10 percent.

Table 2. Variation of Debye parameters for healthy skin fitted to maximum and minimum experimental data.

|	ϵ_∞	$\Delta\epsilon_1$	$\Delta\epsilon_2$	τ_1/ps	τ_2/ps
maximum	2.62	11.96	1.58	1.5	0.0613
minimum	2.55	9.13	1.58	1.4	0.0610
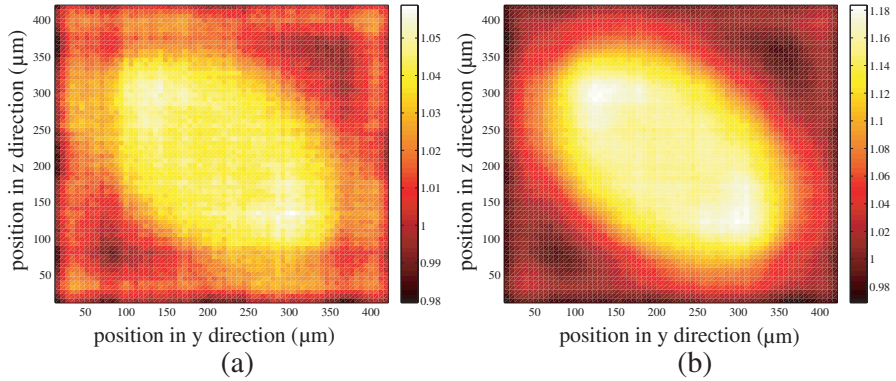
Figure 7. Same as Figure 6, but with added white Gaussian noise of SNR 32 dB to the reflected terahertz pulse.

Next, we consider some variability of Debye parameters in the healthy skin. Note that the Debye parameters for healthy skin in Table 1 is fitted based on the mean value of the data obtained from experiments in [10]. Here, we slightly vary the Debye parameters of the healthy skin to represent the maximum and the minimum values of the experimental data. Such different parameterization may be attributed to different pigmentation level in the healthy skin. The variation of Debye parameters for healthy skin is shown in Table 2. Figure 6 shows the numerically scanned images of the normalized overall post-processed peak-to-peak terahertz pulse of elliptical BCC patch embedded within healthy skin with Debye parameters fitted to (a) maximum and (b) minimum experimental data. We can observe that for BCC patch embedded within healthy skin with Debye parameters fitted to maximum experimental data (c.f. Figure 6(a)), the contrast is reduced to 5 percent compared to a contrast of 10 percent in Figure 4. This is because the maximum experimental data of healthy skin is now closer to that of the BCC in terms of refractive index and absorption coefficient. On the other hand, for BCC patch embedded within healthy skin with Debye parameters fitted to minimum experimental data (c.f. Figure 6(b)), the contrast is increased to around 18 percent compared to a contrast of 10 percent in Figure 4. The minimum experimental data of healthy skin is now further away from that of the BCC. It is also mentioned in [10] that the typical signal-to-noise (SNR) ratio in the system is around 4000 (36 dB). To consider the effect of such noise in the system, we include a white Gaussian noise in the simulated reflected terahertz pulse with the same SNR. Figure 7 shows the same numerical scanned images as in Figure 6, but with white Gaussian noise of 36 dB SNR added to the

reflected terahertz pulse. It can be seen that due to the high SNR, the contrast is not affected and the BCC patch can still be clearly identified under the influence of noise.

In previous numerical examples, the filter function $W(f)$ is selected as a modulated Gaussian to capture the frequency components of the reflected terahertz pulse from 0.2 to 2 THz. It is reported in [10] that a higher percentage difference of refractive index between healthy skin and BCC lies between 0.35 and 0.55 THz. Figure 8 now shows the numerically scanned images of the normalized post-processed peak-to-peak terahertz pulse for (a) BCC patch with circular cross sectional area and (b) BCC patch with 45 degree counter-clockwise rotated elliptic cross sectional area, where the filter function is chosen to only capture the frequency components of the reflected terahertz pulse from 0.35 to 0.55 THz. It can be seen that a higher contrast of 15 percent is exhibited by the BCC patches if we were to extract the reflected terahertz pulse from 0.35 to 0.55 THz. This is consistent with the results in [10] where a higher percentage difference of refractive index between healthy skin and BCC is observed between 0.35 and 0.55 THz.

We now consider the effect of an encrusted layer on top of the BCC patch. The BCC has a thickness of 300 μm and is modeled as a two-layered medium where the bottom layer is the BCC itself with *ex vivo* Debye parameters from Table 1. On top of that, there is an encrusted layer at the top with thickness of 3 μm. A constant
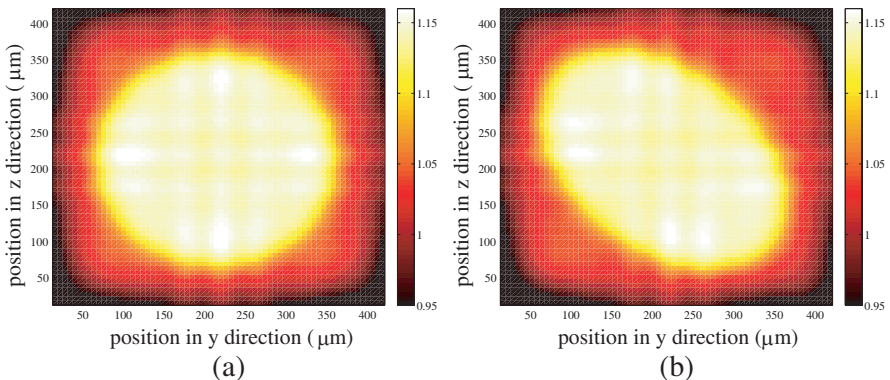
Figure 8. Numerically scanned images of the normalized post-processed peak-to-peak terahertz pulse for (a) BCC patch with circular cross sectional area and (b) BCC patch with 45 degree counter-clockwise rotated elliptic cross sectional area. The filter function is chosen to only capture the frequency components of the reflected terahertz pulse from 0.35 to 0.55 THz.
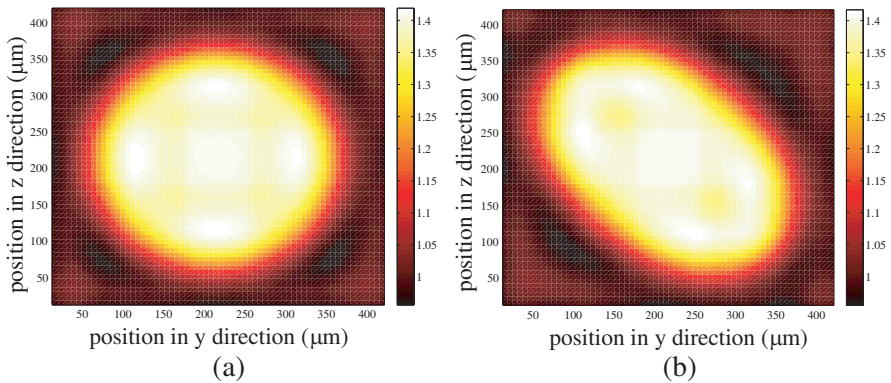
Figure 9. Numerically scanned images of the normalized post-processed peak-to-peak terahertz pulse for (a) BCC patch with circular cross sectional area and (b) BCC patch with 45 degree counter-clockwise rotated elliptic cross sectional area. The BCC patches include the encrusted layer.

relative permittivity, ϵ_r of 3 is assumed for this encrusted layer [14]. In this numerical example we shall adopt a nonuniform cell size along the depth of the skin (x-direction). The $3\,\mu$m-thick encrusted layer is discretized by $\Delta x = 0.6\,\mu$m, while the discretization for rest of the depth layer of the skin remains at $\Delta x = 6\,\mu$m, i.e., the encrusted layer is discretized by cell size 10 times smaller than the rest of the depth layer. $\Delta y = \Delta z = 6\,\mu$m is preserved for the entire computational domain. Due to the unconditional stability feature of FADI-FDTD, the nonuniform cell size will further demonstrate the strengths of our FADI-FDTD since its time step is still unaffected and unrestricted by the usage of a small Δx in the encrusted layer. Figure 9 plots the numerically scanned images of the normalized post-processed peak-to-peak terahertz pulse for (a) BCC patch with circular cross sectional area and (b) BCC patch with 45 degree counter-clockwise rotated elliptic cross sectional area. Both BCC patches include a $3\,\mu$m-thick encrusted layer. It can be seen that the contrast is now as high as 40 percent between the BCC patches and the surrounding healthy skin tissue. The presence of a thin encrusted layer further increases the contrast exhibited by the BCC patches due to the fact that the difference in the refractive index between BCC (with encrusted layer) and quartz is much higher than that of healthy skin and quartz.

For comparison, the numerical example is repeated using the Yee's explicit FDTD method. Note however that the time step of the Yee's explicit FDTD method is restricted by the CFL condition

**Table 3.** Efficiency gain and relative root-mean-square (RMS) error of FADI-FDTD for various CFLNs.

CFLN	Efficiency Gain	Relative RMS Error
4	2.44	2.65 %
10	6.10	6.42 %
15	9.15	8.34 %

in (1). From (1), it is determined that the time step used in the Yee's explicit FDTD method is restricted to 15 times smaller than the original time step used in FADI-FDTD, which corresponds to CFLN = 15 in our FADI-FDTD method. Table 3 further shows the efficiency gain and relative root-mean-square (RMS) error of FADI-FDTD for various CFLNs. The efficiency gain is taken over the Yee's explicit FDTD in terms of CPU run time, while the RMS error is computed by taking the Yee's explicit FDTD as the reference solution. This table gives a clear illustration on the trade-off between accuracy and efficiency of our FADI-FDTD method. For the previous numerical example at CFLN = 15, our FADI-FDTD is 9.15 times faster than the Yee's explicit FDTD method, at the expense of only 8.34 percent RMS error. For a smaller CFLN of 4, our FADI-FDTD is still 2.44 times faster than the Yee's explicit FDTD method, with higher accuracy of 2.65 percent RMS error. This implies that our FADI-FDTD method achieves a good trade-off between efficiency and accuracy.

We further consider the case of a buried BCC tumour. The BCC is now modeled as a sphere with a radius of 150 μm buried within the healthy skin. Note that the reflected peak-to-peak terahertz pulse in all the previous cases can no longer be used directly. To extract the actual reflected terahertz pulse from the buried BCC tumour, we adopt

$$E_{zb}^r = E_z^r - E_{z(ref)}^r \tag{35}$$

where E_{zb}^r is the z-directed reflected electric field from the buried BCC tumour, E_z^r is the z-directed reflected electric field recorded and $E_{z(ref)}^r$ is the reference z-directed reflected electric field, obtained from a confirmed healthy skin. Note that E_z^r consists of reflected terahertz pulse from both healthy skin and buried BCC tumour. Using (35), the desired reflected terahertz pulse from only the buried BCC tumour can be isolated. If the buried BCC tumour is not present, E_{zb}^r will be equal to zero. The post-processing in (32) and (33) are then applied to extract its peak-to-peak E_{zbpp}. Similar procedure is then applied to the y-directed electric field to obtain E_{ybpp}. Finally, the overall
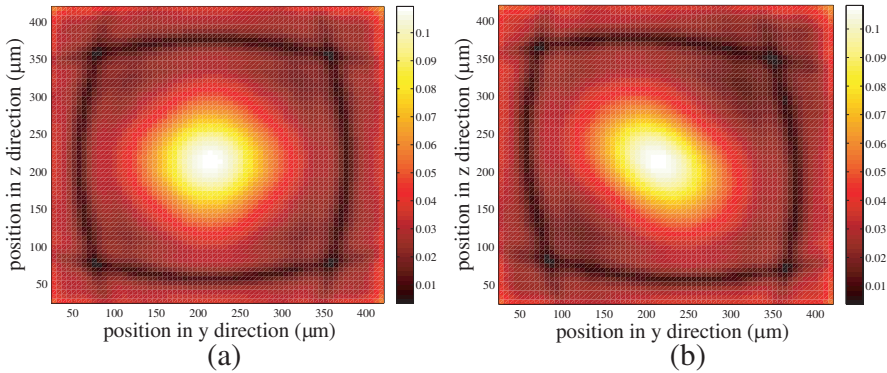
Figure 10. Numerically scanned images of the normalized overall post-processed peak-to-peak terahertz pulse of buried tumour, E_{bpp} with the shape of (a) sphere and (b) 45 degree counter-clockwise rotated ellipsoid. Region with value of zero indicates that of a healthy skin tissue.

post-processed peak-to-peak electric field of buried BCC tumour is

$$E_{bpp} = \frac{1}{2}(E_{zbpp} + E_{ybpp}). \tag{36}$$

Figure 10(a) shows the numerically scanned image of the normalized overall post-processed peak-to-peak terahertz pulse of the buried spherical BCC tumour E_{bpp}. In this case, region with value of zero indicates that of a healthy skin tissue (BCC tumour not present). From Figure 10(a), the buried BCC tumour can still be seen with E_{bpp} of approximately 10 percent more than that of the surrounding healthy tissue. For an ellipsoidal BCC tumour, its semi-principal axes oriented along x, y and z axes have the lengths of 150 μm, 120 μm and 180 μm, respectively. On top of that, it is also rotated 45 degree counter-clockwise along the depth axis. Depicted in Figure 10(b), this buried ellipsoid can also be identified with E_{bpp} of approximately 10 percent more than that of the surrounding healthy tissue. The margin of BCC tumour is smaller compared to the previous cases due the fact that it is buried within the healthy skin.

Based on our simulations shown in Figures 4, 9 and 10, it is noted that the BCC with encrusted layer exhibits higher contrast than that of BCC without encrusted layer. Thus, the presence of encrusted layer further enhances the contrast shown by the BCC. Hereby, the authors would like to point out that it is likely that the considerably good image contrast between the BCC and healthy skin as performed in the experiments in [8, 9] may not be attributed to the BCC and healthy

skin alone. Rather, it is also coupled by the existence of the encrusted layer of the BCC, or perhaps other physical layers within the BCC. Furthermore, during the measurement of the complex refractive index of human skin [10] (from which the Debye parameters are extracted), the skin samples are tightly pressed between the sample holder which may have removed some of the water and intracellular fluid. As water plays an important role in terahertz region where it exhibits high absorption spectra [22], the loss of water and intracellular fluids in the skin during measurement may have caused the discrepancy between measured (and hence the Debye parameter used in numerical experiments) and actual complex refractive index of healthy skin and BCC.

5. CONCLUSION

This paper has presented the application of unconditionally stable FADI-FDTD method in modeling the interaction of terahertz pulse with healthy skin and BCC. The healthy skin and BCC have been modeled as Debye dispersive media and the model is incorporated into the FADI-FDTD method. Numerical experiments on delineating the BCC margin from healthy skin have been demonstrated using the FADI-FDTD method based on reflected terahertz pulse. Hence, the FADI-FDTD provides further insight on the different response shown by healthy skin and BCC under terahertz pulse radiation. Such understanding of the interaction of terahert pulse radiation with biological tissue such as human skin is an important step towards the advancement of future terahertz technology on biomedical applications.

REFERENCES

1. Han, P. Y., G. C. Cho, and X. C. Zhang, "Time-domain transillumination of biological tissues with terahertz pulses," *Opt. Lett.*, Vol. 25, 242–244, 2000.

2. Smye, S. W., J. M. Chamberlain, A. J. Fitzgerald, and E. Berry, "The interaction between terahertz radiation and biological tissue," *Phys. Med. Biol.*, Vol. 46, 101–112, 2001.

3. Pickwell, E. and V. P. Wallace, "Biomedical applications of terahertz technology," *J. Phys. D: Appl. Phys.*, Vol. 39, 301–310, 2006.

4. Son, J.-H., "Terahertz electromagnetic interactions with biological matter and their applications," *J. Appl. Phys.*, Vol. 105, Art. No. 102033, 2009.

5. Woodward, R. M., B. E. Cole, V. P. Wallace, D. D. Arnold, R. J. Pye, E. H. Linfield, M. Pepper, and A. G. Davies, "Terahertz pulse imaging of in vitro basal cell carcinoma samples," *TOPS*, Vol. 56, 329–330, 2001.

6. Woodward, R. M., B. E. Cole, V. P. Wallace, R. J. Pye, D. D. Arnold, E. H. Linfield, and M. Pepper, "Terahertz pulse imaging in reflection geometry of human skin cancer and skin tissue," *Phys. Med. Biol.*, Vol. 47, 3853–3863, 2002.

7. Pickwell, E., B. E. Cole, A. J. Fitzgerald, M. Pepper, and V. P. Wallace, "In vivo study of human skin using pulsed terahertz radiation," *Phys. Med. Biol.*, Vol. 49, 1595–1607, 2004.

8. Wallace, V. P., P. F. Taday, A. J. Fitzgerald, R. M. Woodward, J. Cluff, R. J. Pye, and D. D. Arnone, "Terahertz pulsed imaging and spectroscopy for biomedical and pharmaceutical applications," *Faraday Discuss.*, Vol. 126, 255–263, 2004.

9. Wallace, V. P., A. J. Fitzgerald, S. Shankar, N. Flanagan, R. J. Pye, J. Cluff, and D. D. Arnone, "Terahertz pulsed imaging of basal cell carcinoma ex vivo and in vivo," *British J. Dermatol.*, Vol. 151, 424–32, 2004.

10. Wallace, V. P., A. J. Fitzgerald, E. Pickwell, R. J. Pye, P. F. Taday, N. Flanagan, and H. A. Thomas, "Terahertz pulsed spectroscopy of human basal cell carcinoma," *Appl. Spectroscopy*, Vol. 60, 1127–1133, 2006.

11. Yee, K. S., "Numerical solution of initial boundary value problems involving Maxwell's equation in isotropic media," Vol. 14, No. 4, 302–307, Apr. 1966.

12. Taflove A. and S. C. Hagness, *Computational Electrodynamics: The Finite-Difference Time-Domain Method*, Artech House, Boston, MA, 2005.

13. Pickwell, E., B. E. Cole, A. J. Fitzgerald, V. P. Wallace, and M. Pepper, "Simulation of terahertz pulse propagation in biological systems," *Appl. Phys. Lett.*, Vol. 84, 2190–2192, 2004.

14. Pickwell, E., A. J. Fitzgerald, B. E. Cole, P. F. Taday, R. J. Pye, T. Ha, M. Pepper, and V. P. Wallace, "Simulating the response of terahertz radiation to basal cell carcinoma using ex vivo spectroscopy measurements," *J. Biomed. Opt.*, Vol. 10, Art. No. 064021, 2005.

15. Tan, E. L., "Fundamental schemes for efficient unconditionally stable implicit finite-difference time-domain methods," Vol. 56, No. 1, 170–177, Jan. 2008.

16. Zheng, F., Z. Chen, and J. Zhang, "Toward the development of a three-dimensional unconditionally stable finite-difference time-domain method," Vol. 48, No. 9, 1550–1558, Sep. 2000.

17. Namiki, T., "3-D ADI-FDTD method: Unconditionally stable time-domain algorithm for solving full vector Maxwell's equations," Vol. 48, No. 9, 1743–1748, Oct. 2000.

18. Tan, E. L., "Concise current source implementation for efficient 3-D ADI-FDTD method," Vol. 17, No. 11, 748–750, Nov. 2007.

19. Sandby-Moller, J., T. Poulsen, and H. C. Wulf, "Epidermal thickness at different body sites: Relationship to age, gender, pigmentation, blood content, skin type and smoking habits," *Acta Dermatol. Venereol.*, Vol. 83, 410–413, 2003.

20. Koehler, M. J., T. Vogel, P. Elsner, K. Konig, R. Buckle, and M. Kaatz, "In vivo measurement of the human epidermal thickness in different localizations by multiphoton laser tomography," *Skin Research and Technology*, Vol. 16, 259–264, 2010.

21. Tay, W. C., D. Y. Heh, and E. L. Tan, "GPU-accelerated fundamental ADI-FDTD with complex frequency shifted convolutional perfectly matched layer," *Progress In Electromagnetics Research M*, Vol. 14, 177–192, 2010.

22. Hale, G. M. and M. R. Querry, "Optical constants of water in the 200 nm to 200 um wavelength region," *Appl. Opt.*, Vol. 12, 555–563, 1973.